Heat and Mass Transfer (2019) 55:2857–2872
https://doi.org/10.1007/s00231-019-02615-z

ORIGINAL

Entropy generation analysis of convective turbulent flow in alternating elliptical axis tubes with different angles between pitches; a numerical investigation

Hasan Najafi Khaboshan [1] · Hamid Reza Nazif [1]

Received: 31 October 2018 / Accepted: 4 April 2019 / Published online: 2 May 2019
© Springer-Verlag GmbH Germany, part of Springer Nature 2019

Abstract

This paper presents a numerical analysis for studying entropy generation and the convective turbulent flow of an alternating elliptical axis (AEA) tube with different angles between the pitches at constant wall temperature boundary conditions. The turbulent flow of water fluid is simulated at Reynolds numbers of 10,000 to 60,000. The numerical results indicated that the multi-longitudinal vortices have a major influence on convective heat transfer, pressure drop and entropy generation. Two symmetrical vortices having the same direction of rotation close to the tube wall cause local wall shear stress and the local total entropy generation of the tube wall decrease. However, in some parts of the domain of the AEA tubes, these symmetrical vortices are absent. Therefore, there are different results for the local wall shear stress and the local total entropy generation in all domains of the AEA tubes. The Nusselt number and friction factor increases with an increase in Reynolds number and the angle between pitches of the AEA tube. The entropy generation analysis showed that the main source of irreversibility is by thermal entropy generation. The total entropy generation increases when there is an increase in the Reynolds number, as well as the angle between pitches of the AEA tube. Also, at Reynolds numbers of 20,000, the ratio of the total entropy generation of AEA tube to that of the circular tube is at its minimum.

Nomenclature

A	Area, m^2
A	Major axes length of elliptical cross-section, m
B	Minor axes length of elliptical cross-section, m
C	Transition length, m
C_p	Specific heat, J kg^{-1} K^{-1}
D_h	Hydraulic diameter, m
d	Circular tube diameter of AEA tube, m
f	Friction factor, $f = (\Delta p\, D_h)/\left(\frac{1}{2}\rho\, u_{avg}^2\, L\right)$
g	Gravitational acceleration, m s^{-2}
h	Heat transfer coefficient, W m^{-2} K^{-1}
K	Thermal conductivity, W m^{-1} K^{-1}
k	Turbulent kinetic energy, m^2 s^{-2}
L	Total length of tube, m
L_d	Length of inlet and outlet circular tube, m
Nu	Nusselt number, $Nu = (q''D_h)/(K\,(T_w - T_b))$
P	Pressure, kg m^{-1} s^{-2}
P	Pitch length, m
$\overline{P}$	Mean pressure, kg m^{-1} s^{-2}
P_k	Production of turbulent kinetic energy, kg m^{-1} s^{-3}
Pr	Prandtl number, $Pr = \mu\, C_p/K$
q''	Heat flux, W m^{-2}
Re	Reynolds number, $Re = \rho\, u\, D_h/\mu$
S''_{gen}	Entropy generation, W m^{-3} K^{-1}
S_{gen}	Entropy generation, W K^{-1}
T	Temperature, K
T_b	Average bulk temperature, K
$\overline{T}$	Mean temperature, K
T'	Turbulent temperature fluctuations, K
u_i	Velocity, m s^{-1}
$\bar{u}_i$	Mean velocity, m s^{-1}
u'_i	Turbulent velocity fluctuations, m s^{-1}
x_i	Cartesian coordinates, m
y^+	Dimensionless wall distance, $y^+ = \left(\sqrt{\tau_w/\rho}\, Y\right)/\upsilon$
Y	Distance of the closest computational node from the wall, m
z	Axial distance from inlet, m

✉ Hamid Reza Nazif
nazif@eng.ikiu.ac.ir; h_nazif@yahoo.com

Hasan Najafi Khaboshan
najafi.fme@gmail.com

[1] Department of Mechanical Engineering, Imam Khomeini International University, Qazvin 3414896818, Iran

Greek symbols

δ_{ij} Kroneckr delta
ε Turbulent dissipation rate, $m^2\ s^{-3}$
θ Angle between major axes of elliptical cross-section tubes
μ Laminar dynamic viscosity, $kg\ m^{-1}\ s^{-1}$
μ_t Turbulent dynamic viscosity, $kg\ m^{-1}\ s^{-1}$
μ_{eff} Effective dynamic viscosity, $kg\ m^{-1}\ s^{-1}$
υ Kinematic viscosity, $m^2\ s^{-1}$
ρ Density, $kg\ m^{-3}$
σ_k Turbulent Prandtl number of k equation, σ_k=1
σ_ε Turbulent Prandtl number of ε equation, σ_ε=1.3
τ_{ij} Stress tensor, $kg\ m^{-1}\ s^{-2}$

Subscripts

AEAT Alternating elliptical axis tube
avg Average
CT Circular tube
eff Effective
f Frictional
T Total
th Thermal
w Wall

1 Introduction

Heat exchangers are widely used in many applications of engineering fields such as the petroleum industry, power plant, heating and cooling systems, the automotive industry, etc. Also, it is very important to reduce energy losses in these appliances, so as to improve their efficiency. Several heat transfer enhancement techniques are exploited to increase the heat transfer of heat exchanger systems and it is achieved via two categories, named (i) active and (ii) passive methods.

Active methods utilize external energy sources to enhance the rate of heat transfer by heat exchangers such as using magnetic fields [1–3]. However, passive methods like adding nanoparticles to the working fluid [4–6], increasing the surface area so as to increase the contact between fluid and fins [7, 8] and using baffles [9, 10], twisted tapes [11] or vortex generators [12] inside channels and circular tubes without applying any external energy increases the rate of heat transfer. To increase the heat transfer of heat exchanger devices, the alternating elliptical axis tube (AEA) has been used, which is a kind of passive method for enhancing the heat transfer. This kind of tubes is used in the heat exchanger when the heat transfer is more important than the pressure drop. Li et al. [13] analyzed experimental and numerical convection heat transfer in alternating elliptical axis tubes. They found that at a Reynolds number of 1000, transition occurs from the laminar to the turbulent flow in an AEA tube. The numerical results revealed that the complicated multi-longitudinal vortex structure of the flow which emanated from the secondary flow, improved synergy between velocity and temperature gradient to a large extent. In addition, AEA tubes unlike circular tubes can be used to enhance the heat transfer rate under the identical pumping power. Sajadi et al. [14] studied the experimental and numerical heat transfer and flow resistance of oil flow in AEA tubes with flattened and circular tubes. Their numerical results presented that decreasing the aspect ratio and pitch length, resulted in an increase in heat transfer and pressure drop. Also, it was found that AEA tubes perform better than the flattened or circular ones. Forced convection heat transfer of turbulent flow and entropy generation analysis of the AEA tube have been also investigated using Al_2O_3-water nanofluid by Najafi Khaboshan and Nazif [15]. Their results illustrated that the heat transfer of the AEA tube improves when nanofluid has been used. Furthermore, the heat transfer coefficient of the AEA tube is more than the circular tube under the same nanofluid flow. The entropy generation study showed that the most amount of irreversibility creates by thermal entropy generation.

Entropy generation analysis is a tool for determining the irreversibility of an engineering process and is a famous method for investigating the performance of thermal systems [16]. The determination of entropy generation is also important in enhancing the heat transfer performance of the heat exchanger, because entropy generation is a measure of the destruction of available work of the system [17]. The generation of entropy in various applications have been investigated by several studies such as natural and MHD mixed convection in cavities [18, 19], micro channels [20], pulsating heat pipes [21], shell-and-tube heat exchanger [22], heat sinks [23] and combustion processes [24].

You et al. [25] investigated the effects of alignment method and geometrical parameters on entropy generations for laminar heat transfer augmentation with conical strip inserts in horizontal circular tubes. Their result showed that the tube with non-staggered strips is better at heat transfer and *PEC*s compared with the staggered ones. Also, they found that the rate of entropy generation by the non-staggered strips is smaller than that of the staggered alignment. In addition, the total entropy generation number, is sensitive to the geometry angle and is minimal at the Reynolds number of 600 for the enhanced tube.

Entropy generation has also been investigated in turbulent flows. By using numerical methods, Ko and Wu [26] analyzed the entropy generation induced by turbulent forced convection in a curved rectangular duct with external heating. Their result showed that in aspect ratio one, the entropy generation induced by the frictional entropy generation is concentrated within the regions adjacent to the duct walls. Furthermore, it was found that the entropy generated in the flow fields for all the aspect ratios are dominated by the frictional entropy generation, and the total entropy generation is minimal in the aspect ratio of one.

Siadaty and Kazazi [27] studied on convective heat transfer, entropy generation and pressure drop of two type nanofluids (Cu-water and Al_2O_3-water) in horizontal annular tubes. Their CFD results indicated that the highest and lowest heat transfer rate is obtained with the Cu-water and Al_2O_3-water nanofluids, respectively. In addition, Bejan number analysis showed that the dominant irreversibility is concluded for the frictional and thermal entropy generations in Al_2O_3-water and Cu-water flows, respectively.

Recently, many studies have been conducted on the effect of producing the multi-longitudinal vortex structure of turbulent flows on entropy generation [28, 29]. To the best of the authors' knowledge, studies are yet to be published regarding the entropy generation analysis of forced turbulent convection in AEA tubes. This study investigated a 3D numerical analysis to study the convective heat transfer and entropy generation of AEA tubes with various alternative angles of pitches under the turbulent flow. To compare the overall thermo-hydraulic performance of the AEA tubes, the Nusselt number and friction factor for all tubes are calculated with increasing the Reynolds number. The performance evaluation criterion (*PEC*) has been also calculated. Finally, this study provides an entropy generation analysis for evaluating the performance of convective turbulent flow in the AEA tubes with different rotation angles between pitches. In addition, the variation of total entropy generation along the periphery of the cross-section has been studied for each AEA tube.

2 Mathematical model

2.1 Model description

The AEA tube is constructed with a series of periodic pitches with 40°, 60°, 80° and 90° rotation angles between main axes of elliptical cross-section tubes which are connected by transition zones. Figure 1 illustrations the geometrical construction of the AEA tubes for the various angles of pitches used in the current study. To make the input flow condition identical at the same Reynolds number, the input and output of all AEA tubes are circular with d in diameter and L_d in length, being equal to 16.5 and 34 mm respectively. In this figure the value of A, B, C and P are 20, 13, 6 and 34 mm, respectively and θ is the angle between the main axes of the tubes with elliptical cross-section.

2.2 Governing equations

In the present study, the numerical model of the convective turbulent flow was performed by the finite volume method (FVM). The Continuity, momentum and energy equations of the turbulent flow can be formulated as [30]:

Continuity equation:

$$\frac{\partial \bar{u}_i}{\partial x_i} = 0 \tag{1}$$

Momentum equation:

$$\rho \bar{u}_j \frac{\partial \bar{u}_i}{\partial x_j} = -\frac{\partial \bar{P}}{\partial x_i} + \frac{\partial}{\partial x_j}\left(\mu \frac{\partial \bar{u}_i}{\partial x_j} - \rho \overline{u_i' u_j'}\right) \tag{2}$$

where

$$-\rho \overline{u_i' u_j'} = \mu_t \left(\frac{\partial \bar{u}_i}{\partial x_j} + \frac{\partial \bar{u}_j}{\partial x_i}\right) - \frac{2}{3}\rho k \delta_{ij} \tag{3}$$

Energy equation:

$$\rho C_p \bar{u}_i \frac{\partial \bar{T}}{\partial x_i} = \frac{\partial}{\partial x_j}\left[\left(K + \frac{C_p \mu_t}{Pr_t}\right)\frac{\partial \bar{T}}{\partial x_j} + \bar{u}_i \left(\tau_{ij}\right)_{eff}\right] \tag{4}$$

The third term on the right-hand side of the energy equation represents the viscous dissipation shown in Eq. (5). In addition, the turbulent Prandtl number (Pr_t) is equal to 0.85.

$$\left(\tau_{ij}\right)_{eff} = \mu_{eff}\left(\frac{\partial \bar{u}_j}{\partial x_i} + \frac{\partial \bar{u}_i}{\partial x_j}\right) \tag{5}$$

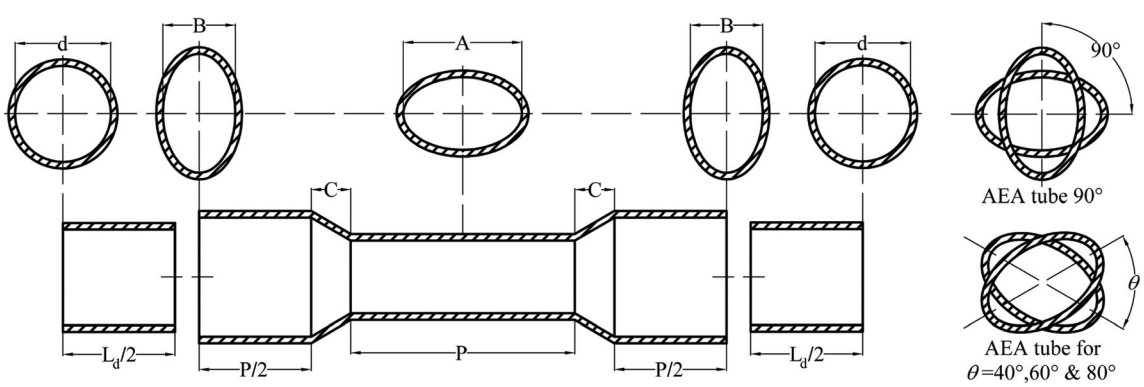

Fig. 1 The geometrical construction of the alternating elliptical axis tube with various alternative angles of pitches

For modeling turbulent flow, it is crucial to select a suitable turbulence model, so as to obtain accurate numerical results. Four common turbulence models are used to investigate the AEA tube simulation are: 1) standard k-ε, 2) realizable k-ε, 3) SST k-ω and 4) the V2F models. By using these models, the numerical results of the average Nusselt number and friction factor of AEA tube 90°, were compared with the experimental data of Guo [31] as presented in Fig. 2. It is evident that the average Nusselt number and friction factor calculated by the k-ε turbulence models are much closer to the experimental data than the other models. Finally, according to these results and previous studies [13, 14, 32–36], the standard k-ε turbulence model is used for numerical simulation of the convective heat transfer of turbulent flow within AEA tubes. Also, the average Nusselt number and friction factor can be written as follows [37]:

$$Nu_{avg} = \frac{1}{L}\int_0^L \frac{q'' D_h}{K(T_w(z) - T_b(z))}\, dz \tag{6}$$

$$f = \frac{\Delta P\ D_h}{\frac{1}{2}\rho u_{avg}^2\ L} \tag{7}$$

Where $T_b(z)$ and ΔP are the average bulk temperature (Eq. (8)) and pressure drop respectively.

$$T_b(z) = \frac{1}{A u_{avg}}\int_A uT\ dA \tag{8}$$

The turbulence kinetic energy (k) and its dissipation rate (ε) equations can be written as [38]:

$$\frac{\partial}{\partial x_i}(\rho k \bar{u}_i) = \frac{\partial}{\partial x_j}\left[\left(\mu + \frac{\mu_t}{\sigma_k}\right)\frac{\partial k}{\partial x_j}\right] + P_k - \rho\varepsilon \tag{9}$$

$$\frac{\partial}{\partial x_i}(\rho \varepsilon \bar{u}_i) = \frac{\partial}{\partial x_j}\left[\left(\mu + \frac{\mu_t}{\sigma_k}\right)\frac{\partial \varepsilon}{\partial x_j}\right] + C_{1\varepsilon}\frac{\varepsilon}{k}P_k - \rho C_{2\varepsilon}\frac{\varepsilon^2}{k} \tag{10}$$

Where μ_t is the turbulent dynamic viscosity, and P_k represents the production of turbulent kinetic.

energy due to the mean velocity gradients.

$$\mu_t = \rho C_\mu \frac{k^2}{\varepsilon} \tag{11}$$

$$P_k = -\rho \overline{u_i' u_j'} \frac{\partial \bar{u}_j}{\partial x_i} \tag{12}$$

The model constants have the following values [38]:

$C_{1\varepsilon} = 1.44, C_{2\varepsilon} = 1.92, C_\mu = 0.09, \sigma_k = 1$ and $\sigma_\varepsilon = 1.3$

The enhanced wall treatment scheme has been applied to simulation the near wall manner of turbulent flow which used a modified formulation for near wall viscosity. The equations of this scheme had been presented in Ref. [32].

2.3 The Boundary conditions

The boundary conditions of velocity inlet and outflow have been selected for the inlet and outlet of tubes, respectively. In the outflow boundary condition, zero-gradient of the flow factors have been considered which are located normal to the outlet boundary of tubes. In addition, at the inlet of the tubes, the velocity parameter has been considered uniform and normal to the inlet section of tubes. The value of the velocity for the inlet boundary condition is calculated from the equation of the flow's Reynolds number. In the equation of

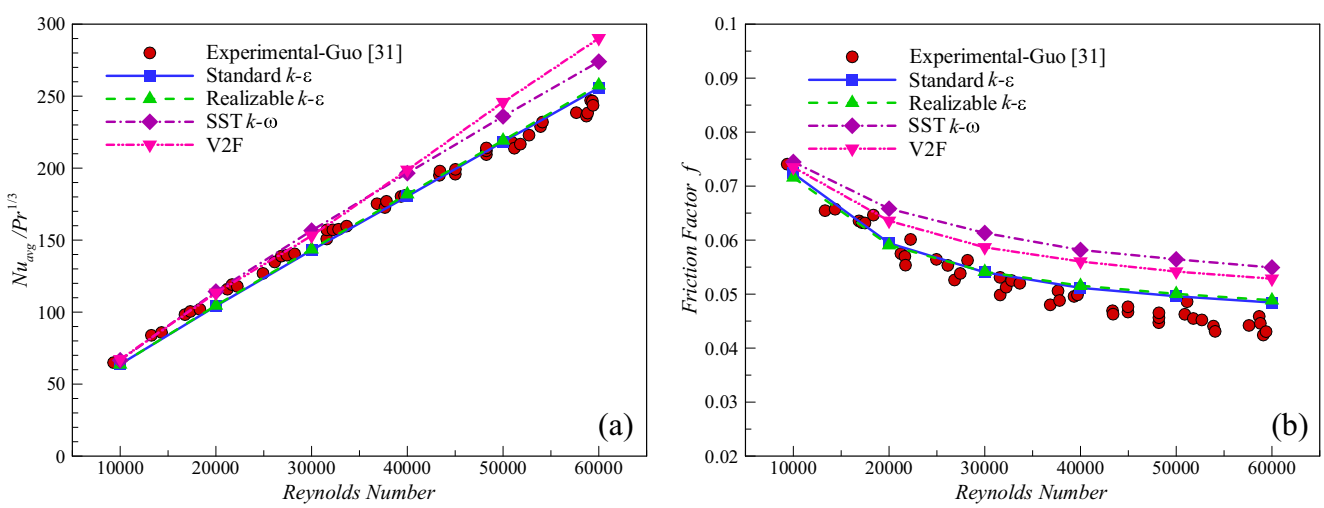

Fig. 2 Validation of turbulence models by comparing the numerical results of **a** average Nusselt number and **b** friction factor with experimental results of Guo [31] in AEA tube 90°

Reynolds number, the diameter of the circular tube (d = 16.5 mm) has been considered for the hydraulic diameter. In Guo's research [31], the difference between the minimum and maximum temperature was fewer than 30 degrees. Therefore, according to this, the inlet temperature is about 295 K. Also, the wall temperature boundary condition has been considered constant and it is equal to 325 K. In addition, the no-slip boundary condition situation has been applied along the wall of the tubes.

2.4 Entropy generation analysis

The second law of thermodynamics is mentioned whenever the basic principles of convective heat transfer are considered. This is simply because it is the basis for much of the engineering motives for formulating and solving convection problems [39]. The second law of thermodynamics is related to entropy generation, and in terms of calculations, it is more reliable than the first law [17]. According to the study by Bejan [40], the local entropy generation can be calculated at every point of the system based on the second law of thermodynamics by the following equation:

$$S'''_{gen,T} = \frac{K}{T^2}\left[\left(\frac{\partial T}{\partial x}\right)^2 + \left(\frac{\partial T}{\partial y}\right)^2 + \left(\frac{\partial T}{\partial z}\right)^2\right] + \frac{\mu}{T} \times 2\left[\left(\frac{\partial u}{\partial x}\right)^2 + \left(\frac{\partial v}{\partial y}\right)^2 + \left(\frac{\partial w}{\partial z}\right)^2\right] + \left(\frac{\partial u}{\partial y} + \frac{\partial v}{\partial x}\right)^2 + \left(\frac{\partial v}{\partial z} + \frac{\partial w}{\partial y}\right)^2 + \left(\frac{\partial w}{\partial x} + \frac{\partial u}{\partial z}\right)^2 \quad (13)$$

The above equations show that the gradients of velocity and temperature must be known at the relevant point in the domain. Since the velocity and temperature fields are known in the domain, the velocity and temperature gradients can be calculated. The gradients of velocity and temperature have been discretized with the green gauss node based [41, 42] scheme. Therefore, the amount of the total entropy generation is available in cells' center of the domain. In Eq. (13), the first term which is the thermal entropy generation ($S'''_{gen,th}$) is connected with heat transfer due to gradients of temperature and the second term represents the frictional entropy generation ($S'''_{gen,f}$) linked to fluid friction irreversibility as a result of the gradients of velocity.

In this research, the value of the entropy generation has been calculated in some cross-sections of tubes and in the domain. The Eqs. (14–16) are considered for computing the entropy generation in each cross-section.

$$S'''_{gen,th} = \frac{1}{A}\int S'''_{gen,th}\ dA = \frac{1}{A}\sum_{i=1}^{n} S'''_{gen,th}(x_i, y_i, z_i)\ \delta A_i \quad (14)$$

$$S'''_{gen,f} = \frac{1}{A}\int S'''_{gen,f}\ dA = \frac{1}{A}\sum_{i=1}^{n} S'''_{gen,f}(x_i, y_i, z_i)\ \delta A_i \quad (15)$$

$$S'''_{gen,T} = \frac{1}{A}\int S'''_{gen,T}\ dA = \frac{1}{A}\sum_{i=1}^{n} S'''_{gen,T}(x_i, y_i, z_i)\ \delta A_i \quad (16)$$

In addition, the entropy generation in the unit of (W/K) to present the results in the domain, can be calculated easily by integrating $S'''_{gen,th}$, $S'''_{gen,f}$ and $S'''_{gen,T}$ over the computational domain as follows, respectively:

$$S_{gen,th} = \int S'''_{gen,th}\ dV = \sum_{i=1}^{n} S'''_{gen,th}(x_i, y_i, z_i)\ \delta V_i \quad (17)$$

$$S_{gen,f} = \int S'''_{gen,f}\ dV = \sum_{i=1}^{n} S'''_{gen,f}(x_i, y_i, z_i)\ \delta V_i \quad (18)$$

$$S_{gen,T} = \int S'''_{gen,T}\ dV = \sum_{i=1}^{n} S'''_{gen,T}(x_i, y_i, z_i)\ \delta V_i \quad (19)$$

To study the weight of each contribution ($S_{gen,th}$ and $S_{gen,f}$) to the total entropy generation, a dimensionless parameter named Bejan number (Be) is defined as [40]:

$$Be = \frac{S_{gen,th}}{S_{gen,T}} \quad (20)$$

Obviously, the value of Be is in the range from 0 to 1. The value of $Be = 0$ and $Be = 1$ indicates that irreversibility is dominated by fluid friction and heat transfer, respectively.

3 Numerical method

For handling the pressure-velocity coupling of the continuity and momentum equations, the SIMPLEC algorithm is employed [43]. The governing equations are calculated with considering the pressure-based coupled algorithm [44]. The gradients of the solution variables of grids for the turbulence and energy equations are considered by least squares cell based (LSCB) [45] and green gauss node based (GGNB) [41, 42] schemes, respectively. Therefore, the energy equation is computed, while the results of the solved turbulent flow are

considered to be frozen. The standard method [45] for solving the pressure of the cell-face has been considered. Also, to discretize all equations, the second-order upwind [46] scheme has been applied. The enhanced wall treatment method [47] has been used to consider the near wall phenomena of the turbulent flow. In this study, the dimensionless parameter of the first near wall cell center which is called y^+ have a value of about one or less than one. Also, variables are stored with double precision, and all the convergence criteria for all equations are considered lower than 10^{-6}.

4 Numerical computation

4.1 Grid independence study

In this study, all grids were generated by using the multi-block scheme with hexahedral elements, as shown in Fig. 3. For all tubes, in order to study the effects of grid size on the numerical results, five three-dimensional grids were generated. Table 1 lists the average Nusselt number (Nu_{avg}) in five computational grids of AEA tube 90° under the turbulent flow of water fluid at $Re = 40{,}000$. From Table 1, it can be seen that the relative error of the average Nusselt number between mesh-4 and mesh-5 is only 0.98320. Therefore, the grid size of mesh-4 (3,951,360 cells) was adopted as the optimal grid size for the numerical simulation of AEA tube 90°.

Table 1 Grid independence study in terms of average Nusselt number

Mesh (number of cells)	Nu_{avg}	$\delta\ Nu_{avg}$
Mesh-1 (1,444,608)	280.9442	–
Mesh-2 (1,932,800)	339.2751	−58.3309
Mesh-3 (3,379,376)	343.5931	−4.31800
Mesh-4 (3,951,360)	345.0233	−1.43020
Mesh-5 (4,646,340)	346.0065	−0.98320

4.2 Computational validation of numerical results

To validate the computational model, the numerical results of the AEA tube 90° and circular tube had been compared with the experimental result and standard correlations, respectively. Guo [31] analyzed the improvement of heat transfer in the AEA tube 90° by using water as the working fluid under the turbulent flow. In this study, the geometrical parameters of his tubes were used. Figure 4 shows the comparisons between the numerical average Nusselt number and the friction factor of an AEA tube 90° with the available experimental data from Guo [31] and numerical research of Chen et al. [36]. Figure 4 demonstrations that the numerical results of the present study correspond with the experimental data of Guo [31]. The maximum errors observed between the experimental and numerical results for the average Nusselt number and friction factor of AEA tube 90° are about 6.5% and 14%, respectively. These maximum absolute deviations for the AEA tube 90° are less than the results reported by Sajadi et al. [14] (i.e., 24% and 21% for the Nusselt number and friction factor, respectively).

By comparing with the experimental results shown in Fig. 4, the average Nusselt number and friction factor obtained by the GGNB and LSCB approaches appear to be suitable for calculating the gradients of the solution variables of energy and turbulent flow equations, respectively. Therefore, these methods are used for the numerical simulation of the AEA tubes. To comparison of the existing numerical results with the previous study [36] which has been examined numerically, the summary of Nusselt number and friction factor of both numerical results are presented in Table 2. In this Table, the values of the experimental results [31] have been obtained as approximately. According to Table 2, it can be found that there is no significant difference between both numerical results and experimental data at the low Reynolds number. In addition, it shows that the numerical method of the present study offers suitable numerical results in comparison with the previous study.

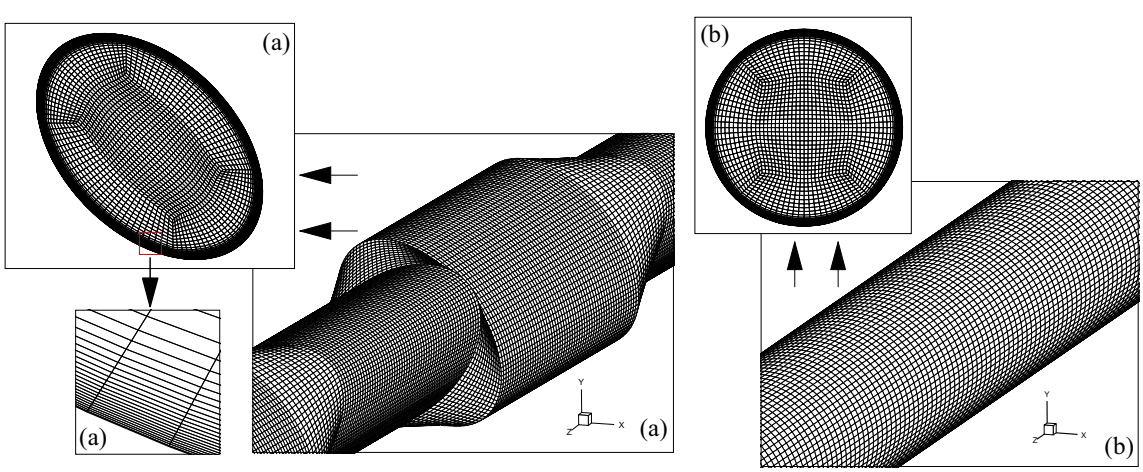

Fig. 3 Grids generated of **a** AEA tube 90° and **b** circular tube in the present numerical computation

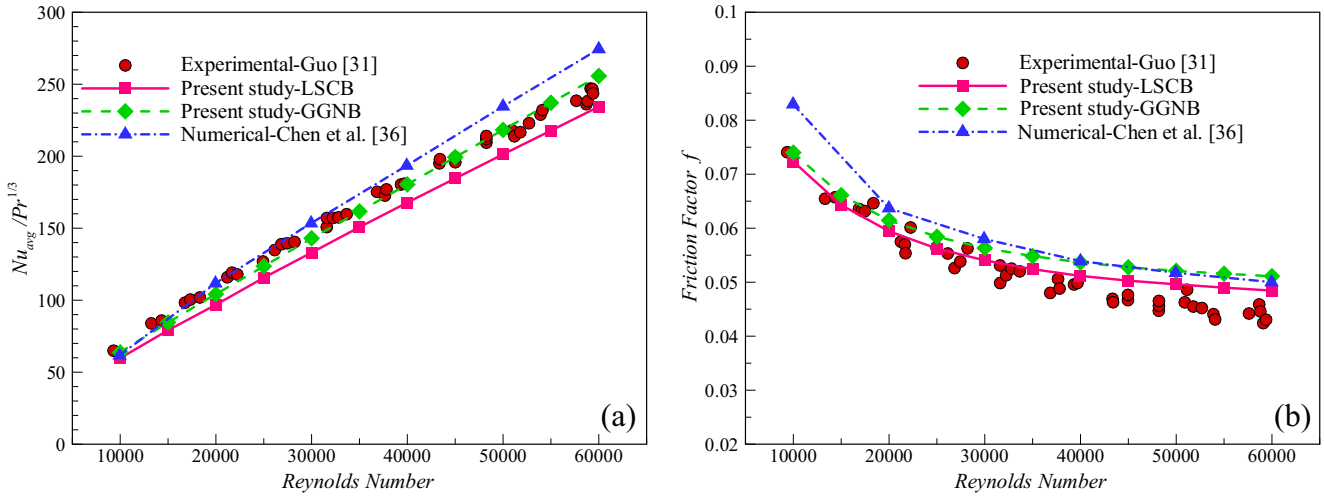

Fig. 4 Comparisons between the numerical results of **a** average Nusselt number and **b** friction factor with the experimental data by Guo [31] and numerical data by Chen et al. [36] for the AEA tube 90°

To validate the numerical simulation of the circular tube, the numerical results were compared with the standard correlation proposed by Gnielinski [48, 49] and Petukhov et al. [50], for the Nusselt number and the friction factor, respectively. Figure 5 shows the comparisons between the numerical results (after fully developed flow) and correlations. It is evident that the numerical results obtained from the circular tube agree well with those correlations.

5 Results and discussion

This section presents turbulent heat transfer and entropy generation of flow in the AEA tube with various angles of pitches. In all numerical simulations of the present study, water was used as the working fluid. Prior to the examination of entropy generation, pressure drop and heat transfer of turbulent flow were discussed in detail.

In our simulation, because of the repeating manner of the solution, the results are illustrated in the parts of the tube that are located in the range of 0.357 to 0.437 m (Fig. 6). In our area of focus for demonstrating the results, three regions were named "Distance A", "Transition" and "Distance B" which are shown in figures of this paper to make it easier to address the readers. Also, in the area shown in Fig. 6, three sections were selected as perpendicular to the flow named as Location A, B and C.

5.1 Local heat transfer coefficient and wall shear stress distribution

Prior to discussing about the local heat transfer coefficient and wall shear stress results, it is necessary to discuss the flow structure of AEA tubes with various rotation angles of θ. To capture the flow structures inside AEA tubes, the streamlines at Location C of all the AEA tubes were investigated in Fig. 7. Also, it is necessary to mention that the numbers shown in Fig. 7, represent the node numbers around the peripheral cross-section of Location C which is illustrated by red points in this figure. As can be observed, fluids flow inside AEA tubes 40° and 60° have four multi-longitudinal vortices at some part of the constant cross-section of the AEA tubes. Furthermore, by increasing the angle of θ from 60° to 80°, secondary flows divide from four to eight and their size becomes smaller compared to the multi-longitudinal vortices of AEA tubes 40° and 60°.

The heat transfer coefficient and wall shear stress (which is related to pressure drop) are two important parameters that should be investigated when studying heat exchangers. The variation of the local heat transfer coefficient and wall shear stress on the circumference of the AEA tubes at Location C, is shown in Fig. 8. The horizontal axes of these figures represent the node numbers of the mesh that was taken in the clockwise direction (from left to right) on the periphery of the elliptical cross-section in the X–Y plane. It should be noted that due to

Table 2 Comparison of the numerical results of the present study and previous research [36]

Reynolds number	$\frac{Nu_{avg}}{Pr^{1/3}}$ experimental	$\frac{Nu_{avg}}{Pr^{1/3}}$ present study	$\frac{Nu_{avg}}{Pr^{1/3}}$ previous study	f experimental	f present study	f previous study
method	–	GGNB	GGNB	–	LSCB	LSCB
20,000	109.66	103.87	111.54	0.06037	0.05938	0.06365
50,000	216.59	218.44	234.79	0.04635	0.04959	0.05172

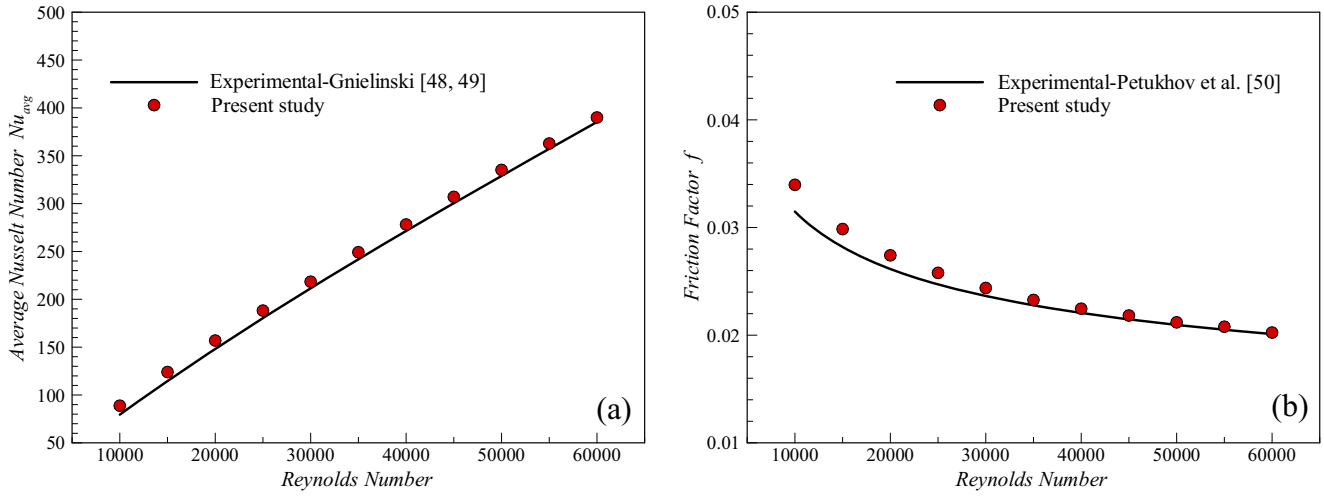

Fig. 5 Comparisons between the numerical results of **a** average Nusselt number and **b** friction factor with correlation proposed by Gnielinski [48, 49] and Petukhov et al. [50], respectively, for a circular tube

the symmetry in the flow structure of this part of the tube, the values of parameters in only half of the periphery of the tube cross-section are shown. It is obvious from Fig. 8a that the local heat transfer coefficient increases around the node numbers 12 and 44 for AEA tube 60°, 80° and 90°. The results are different for AEA tube 40°, and the highest values of heat transfer are located at node numbers 28 and 51. Meanwhile, the local heat transfer coefficient is calculated from Eq. (21).

$$h = \frac{q''}{(T_w - T_b)} \tag{21}$$

Where, q'' is the heat flux on the tube wall, T_w and T_b are the wall temperature and bulk temperature of the fluid, respectively. The bulk temperature is calculated as follows:

$$T_b = \frac{1}{Au_{avg}} \int_A uT \ dA \tag{22}$$

Similarly, from Fig. 8b the local wall shear stress is minimum for AEA tubes 80° and 90° around the node numbers 0, 28 and 56. By comparing Figs. 8b and 7, it can be seen that near the wall of AEA tubes 80° and 90° between two symmetrical vortices with the same direction of rotation, the local wall shear stress is nearly minimum. These two symmetrical vortices are marked with red dash lines in Fig. 7 for AEA tubes 80° and 90°. The local wall shear stress increased around node numbers 14 and 43 for AEA tube 80° and 90°. On the other hand, for AEA tube 40° minimum is seen at node numbers 6 and 37, but for AEA tube 60° the minimum is seen at node numbers 7 and 28.

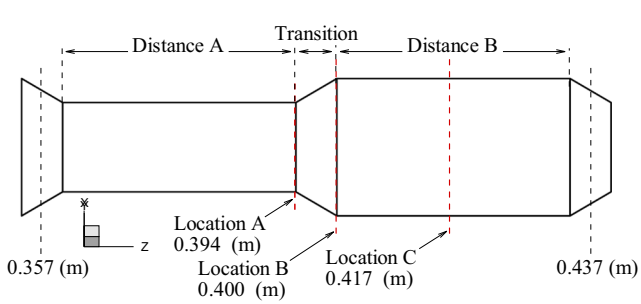

Fig. 6 The situations of the three different locations

To investigate the average heat transfer coefficient and wall shear stress, these two parameters are shown along the specific range of axial direction for all AEA tubes in Figs. 9a and b, respectively. It is obvious that both parameters have a high value in the transition zone, especially at its outlet section. Also, it is clear from Fig. 9a that the difference in the value of average heat transfer coefficient in the inlet and outlet sections of the transition zone for AEA tube 90° is very high compared to other AEA tubes. Similarly, such a difference is observed for the average wall shear stress. It was also observed that the increase in angle θ has a great effect on increasing the heat transfer in some distance of the tube, but the wall shear stress does not change much, except for the AEA tube 90°.

According to these results, it can be determined that the multi-longitudinal vortices have a substantial impact on increasing the heat transfer of turbulent flow. Furthermore, an increase in the number of multi-longitudinal vortices results to improve heat transfer.

5.2 Flow field and wall heat flux distribution

To reveal the flow structure in the AEA tube for different angle of θ, it is useful to investigate the velocity field and streamlines inside the AEA tubes. Figure 10 presents the velocity distributions and streamlines of the AEA tubes along the specific range of the axial direction (0.357 to 0.437 m) in different angle of θ. The streamlines in the transition zone have shifted gradually with increasing the angle of θ. It can be observed from Fig. 10 that the streamlines are almost

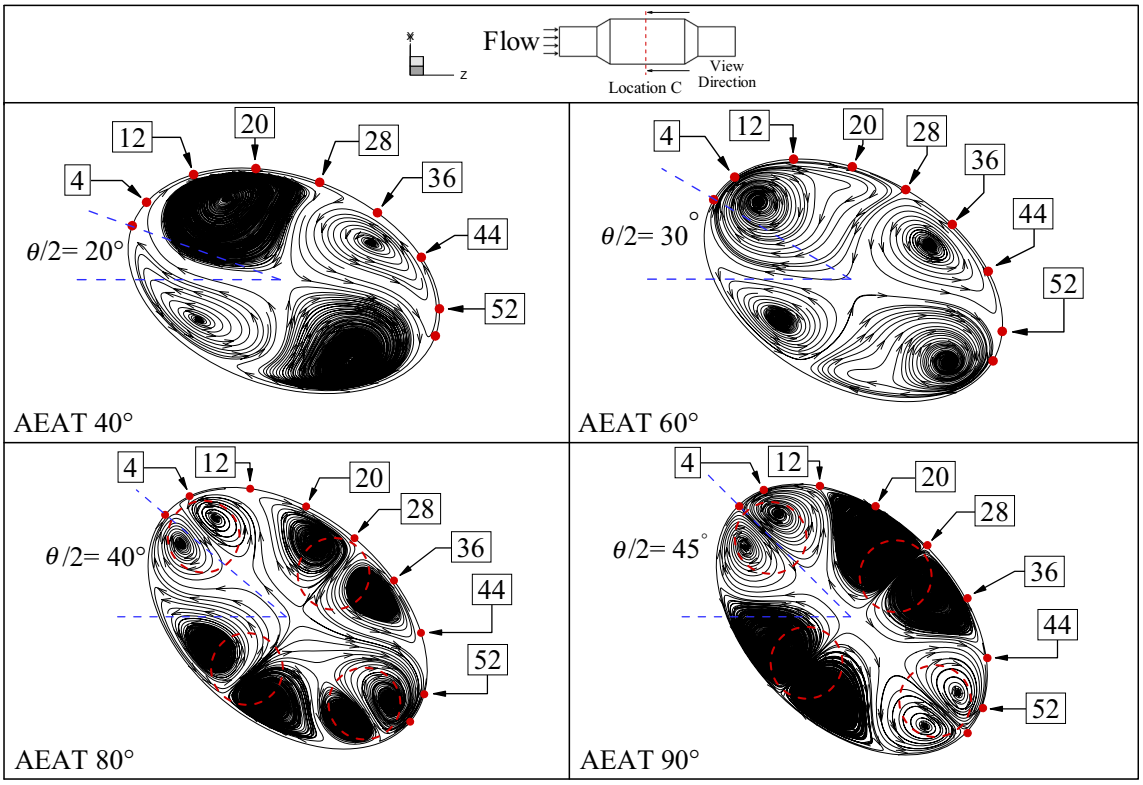

Fig. 7 Streamlines in Location C of all AEA tubes at $Re = 40{,}000$

straight in the AEA tube 40°. Furthermore, the distribution of velocity in the different cross-sections is approximately homogeneous inside the AEA tube 40°. With raising the angle of θ, the velocity contour of cross-sections is changed due to the generated secondary flows, especially at the transition zone.

The wall heat flux distributions of the AEA tubes for the various angle of θ are presented in Fig. 11 to study on heat transfer of turbulent flow within the AEA tubes. It can be seen from this figure that the wall heat flux increases with an increase in the angle of θ. In addition, Fig. 11 shows that the heat

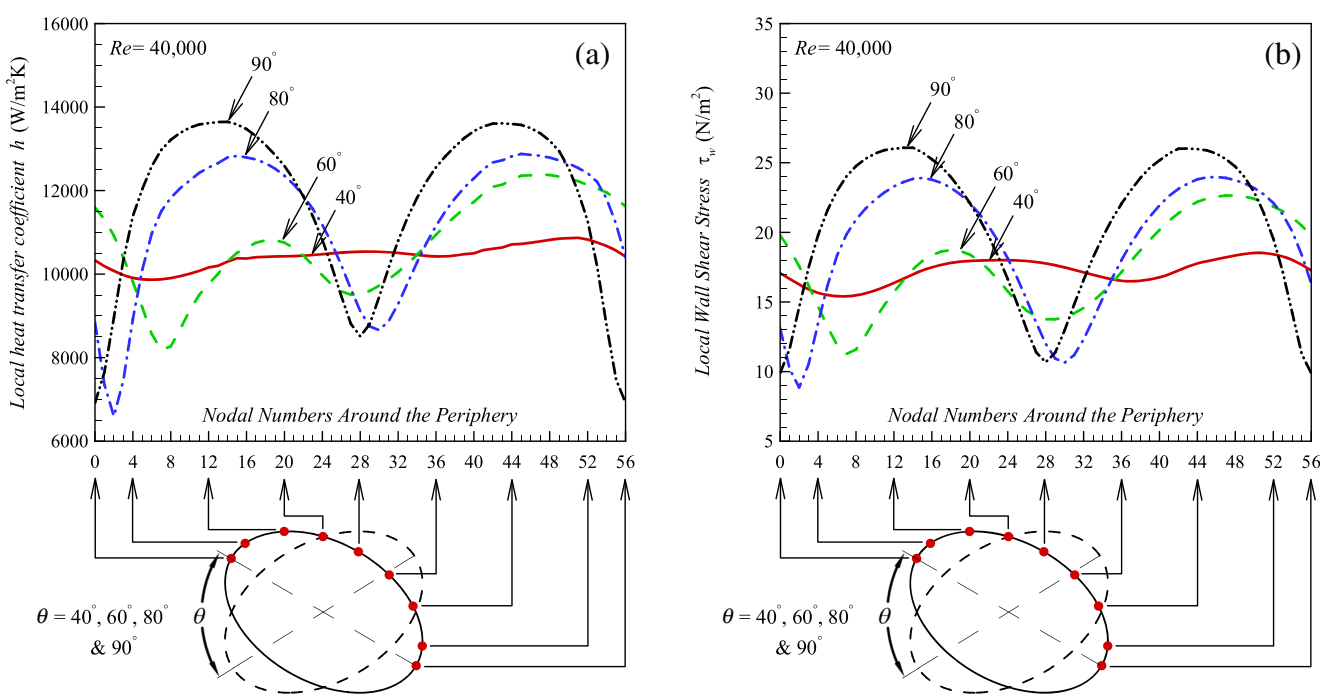

Fig. 8 **a** Local heat transfer coefficient and **b** local wall shear stress variation along the periphery of AEA tubes at Location C

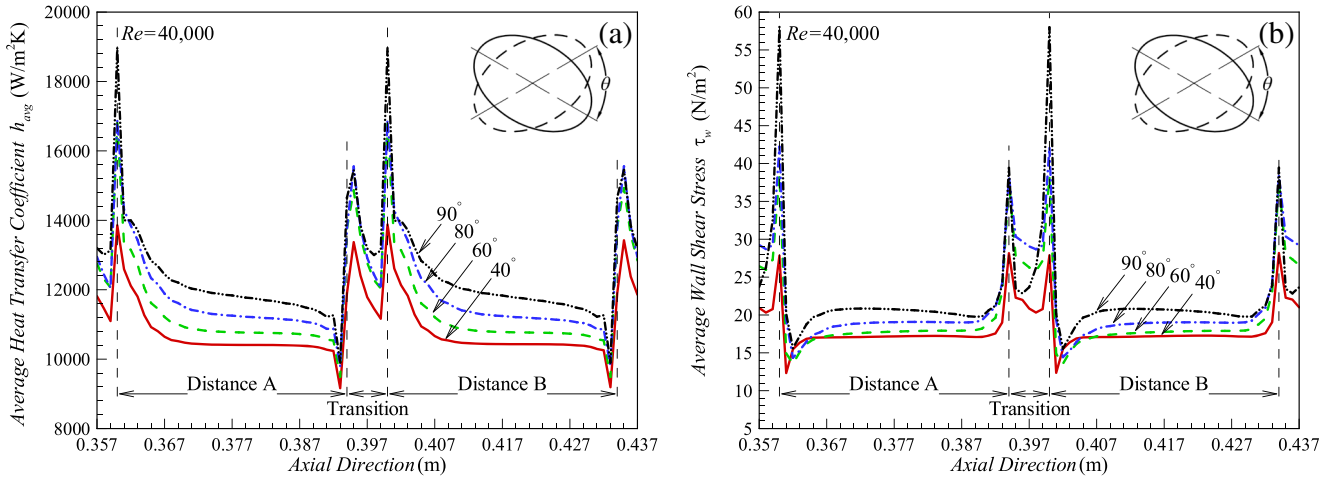

Fig. 9 **a** Average heat transfer coefficient and **b** average wall shear stress along the axial direction of AEA tubes with various angles of θ

transfer of transition zones are greater than the other areas. This is because of forming the multi-longitudinal vortices in the transition zones.

5.3 Average Nusselt number and friction factor distribution

Figures 12a and b show the effect of changing the rotation angle of θ and Reynolds number on the average Nusselt number and friction factor respectively, for all AEA tubes and circular tube. The numerical results are calculated at Reynolds numbers of 10,000 to 60,000. As can be seen from Fig. 12a, the average Nusselt number increases with an increase in Reynolds number for the circular tube as well as all the AEA tubes. It can be found that the convection heat transfer coefficient is increased with increasing the Reynolds number. This is due to the fact that the normal gradient of temperature at the tube wall has been increased with increasing the Reynolds number. Furthermore, compared to the circular tube, the Nusselt number enhancement of the AEA tubes with the angle of 40°, 60°, 80°, and 90° are around 7.77%, 14.6%, 16.93%, and 24.42%, respectively. Also, at a fixed Reynolds number, the average Nusselt number increases with an increase in angle of θ because of increasing the multi-

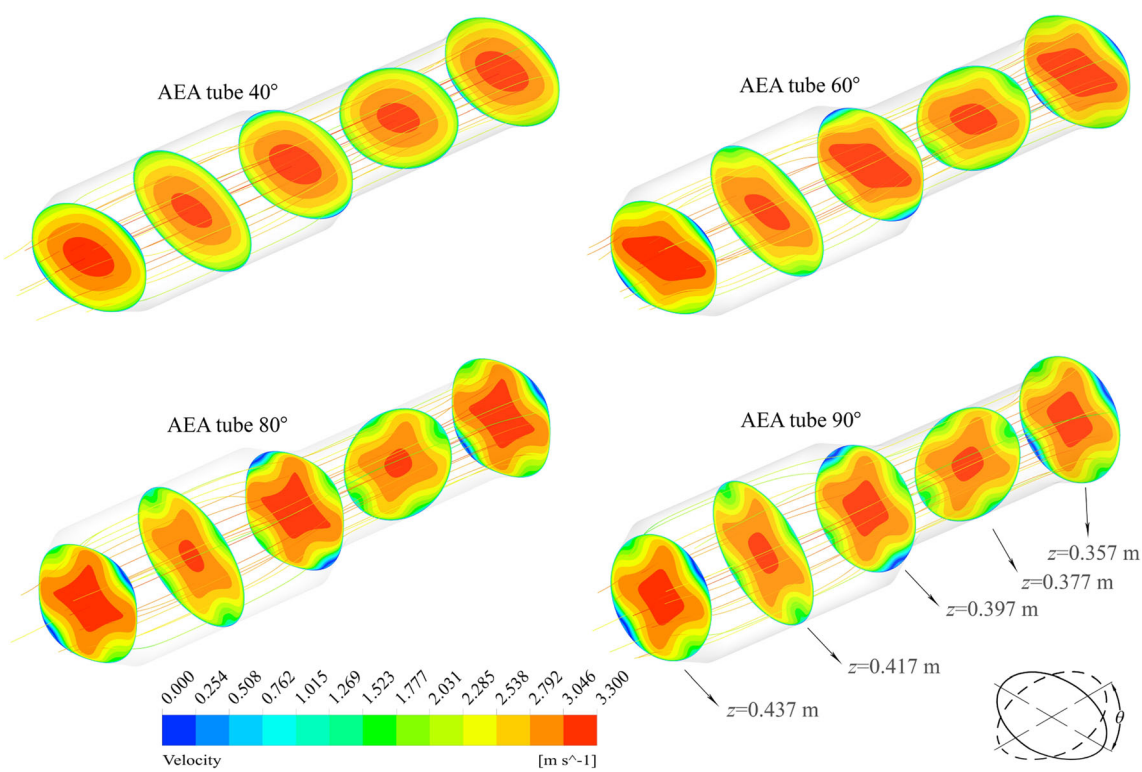

Fig. 10 Velocity distributions and streamlines of the AEA tubes with the various angle of θ at $Re = 40{,}000$

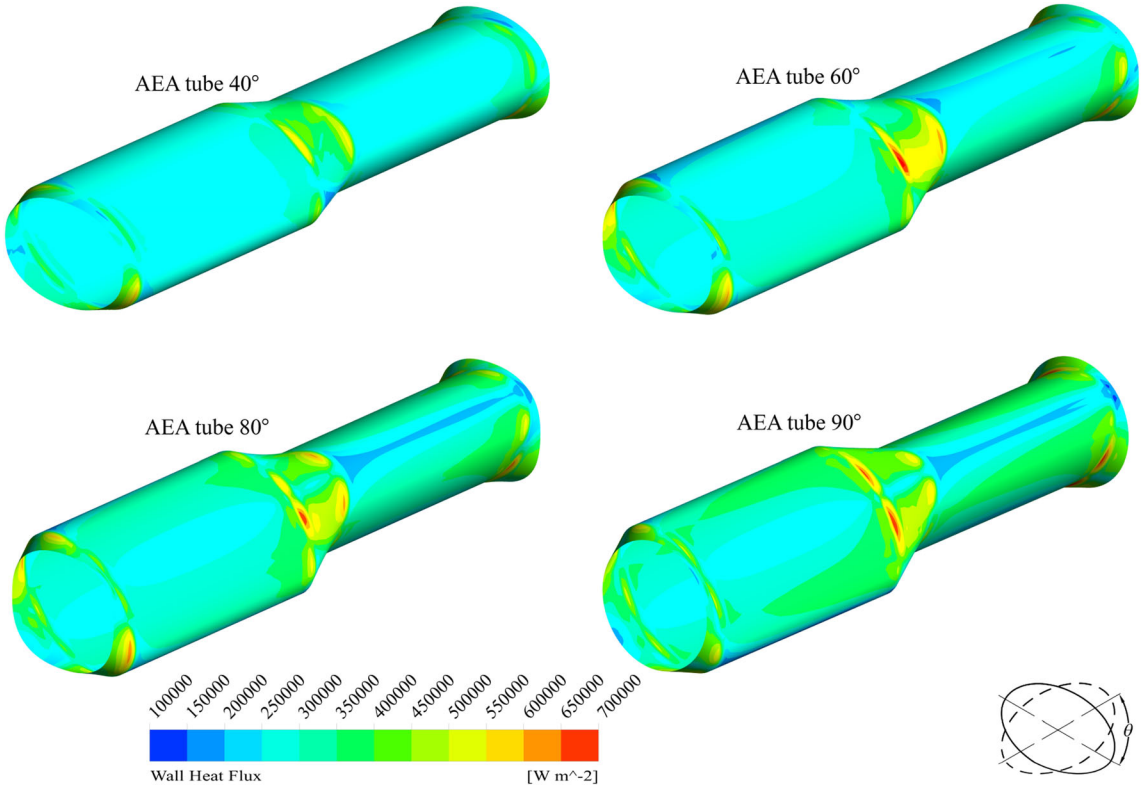

Fig. 11 Wall heat flux distributions of the AEA tubes with the various angle of θ at $Re = 40{,}000$

longitudinal vortices (secondary flows) within the turbulent flow. Similarly, it is obvious from Fig. 12b that the friction factor decreases with increasing the Reynolds number in the circular tube as well as in all the AEA tubes. Also, increasing the angle of θ causes an increase in the friction factor value which is resulted from effects of the secondary flows.

The performance evaluation criterion (*PEC*) has been developed by Webb and Kim [51] to assess the overall thermal-hydraulic performance of the improved tubes at the same power of pumping. The *PEC* has been calculated as below:

$$PEC = \frac{Nu/Nu_s}{(f/f_s)^{1/3}} \tag{23}$$

where Nu_s and f_s are defined as the Nusselt number and friction factor of the base tube, respectively.

The variation of the *PEC* as a function of *Re* is presented in Fig. 13 for the AEA tubes. From this figure, it can be found that the *PEC* values of AEA tubes are fewer than one for $Re \geq 20{,}000$. In addition, the maximum value of the *PEC* for each AEA tube has been acquired at a small Reynolds number. At

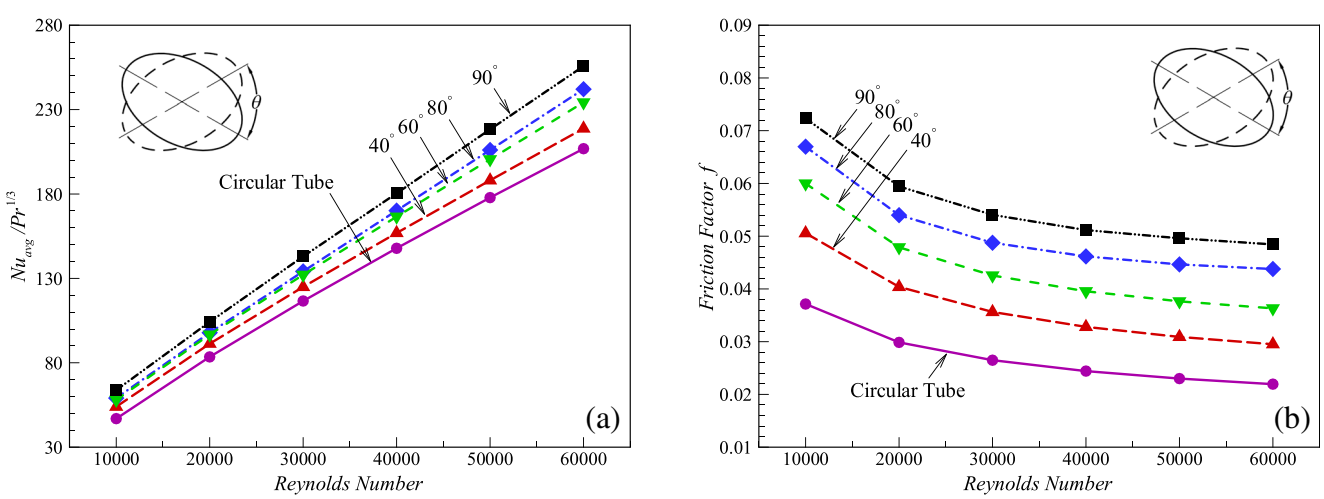

Fig. 12 Effect of changing rotation angle of θ and Reynolds number on **a** average Nusselt number and **b** friction factor

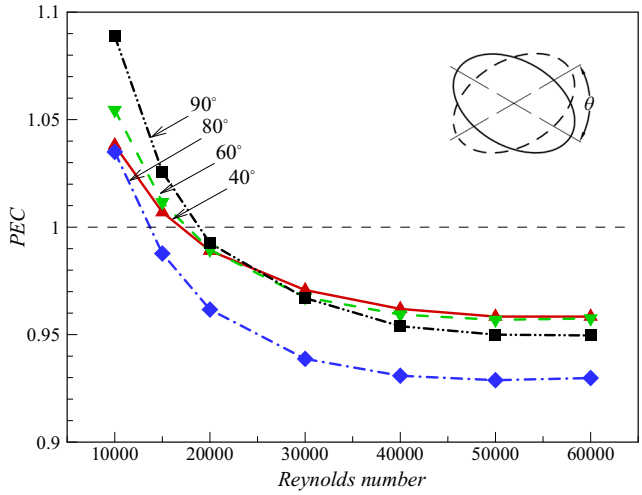

Fig. 13 The performance evaluation criterion (*PEC*) as a function of Reynolds number for the AEA tubes with different angles of θ

Reynolds number of 10,000, the *PEC* raised with raising the angle of θ (except for the AEA tube 80°). The maximum value of the *PEC* (1.09) is obtained in the AEA tube 90° for the smallest Reynolds number, which shows that the AEA tube 90° is more efficient than the circular tube. Finally, it could be reached to the fact that raising the number of multi-longitudinal vortices of the flow with raising the angle of θ cause to improves the heat transfer in comparison with smaller values of angle θ.

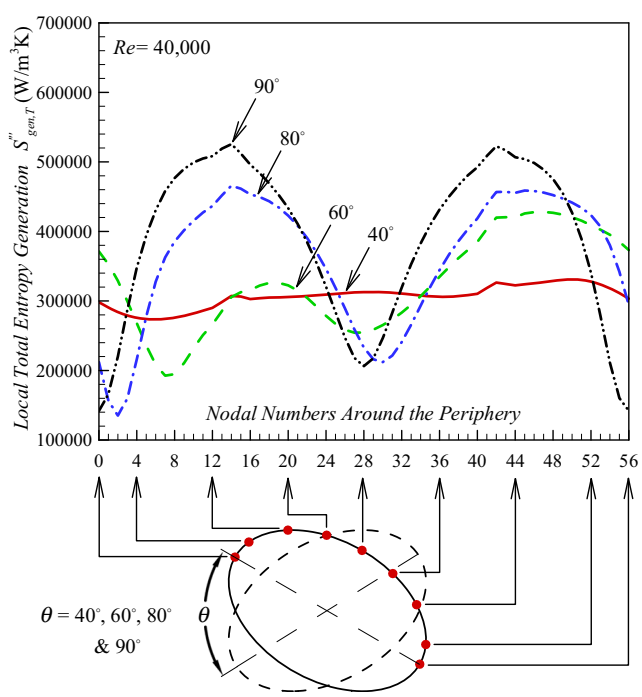

Fig. 14 Local total entropy generation variation of all AEA tubes along the periphery of the cross-section at Location C

5.4 Entropy generation distribution

Figure 14 presents the local total entropy generation of all AEA tubes along the periphery of the cross-section at Location C. From Fig. 14, it can be seen that the local total entropy generation varies as the local heat transfer coefficient. Around node numbers 0, 28 and 56 for AEA tube 80° and 90°, the local total entropy generation has the smallest value compared to other areas. From Figs. 14 and 7, the minimum of the local total entropy generation is seen near the wall of AEA tube 80° and 90° in which two symmetrical vortices are formed with the same direction of rotation. So, in this case, by increasing the number of multi-longitudinal vortices that have two symmetrical vortices with the same direction of rotation, more points are created where the total entropy generation is minimal. Unfortunately, just some portion of the AEA tube have these symmetrical vortices. Therefore, this rule cannot be considered as a general rule for every domain of the AEA tube. Conversely, for the two AEA tubes 40° and 60°, this principle cannot be provided because of the non-symmetry of vortices. For AEA tube 40°, node numbers with the least total entropy generation are very difficult to detect on the tube wall, but at node numbers 7 and 27 for AEA tube 60° minimum is seen.

For further analysis, the effect of different angles of θ on average thermal, frictional and total entropy generation along the specific range of axial direction are shown in Figs. 15a, b and c, respectively. Figure 15a shows that by increasing the angle of θ, there was a significant increase in the average thermal entropy generation in the transition zone. This is because of the biggest temperature gradients on this zone which are according to the presence of the highest heat transfer coefficient (see Fig. 9a). Similarly, as shown in Fig. 15b, by increasing the angle of θ, the average frictional entropy generation is increased as a result of the high values of velocity gradient at the transition zone. In addition, both parameters increased with an increase in the angle of θ at constant cross-sections of the AEA tubes. It is also clear that the variations of the total entropy generation are almost near the variations of thermal entropy generation, and it can be concluded that the effect of thermal entropy generation is several times greater than frictional entropy generation.

To study the effect of Reynolds number on the entropy generation of AEA tubes and the circular tube, the variations of thermal, frictional and total entropy generation with Reynolds number are represented in Fig. 16. According to the results shown in Figs. 16a, b and c, it can be seen that thermal, frictional and total entropy generation are enhanced when the Reynolds number is enhanced in all the tubes. It was also observed that all three parameters of entropy generation of the AEA tubes are greater as compared to the circular tube. Finally, Fig. 16d shows the variations of Bejan number when the Reynolds number is increased for AEA tubes and circular

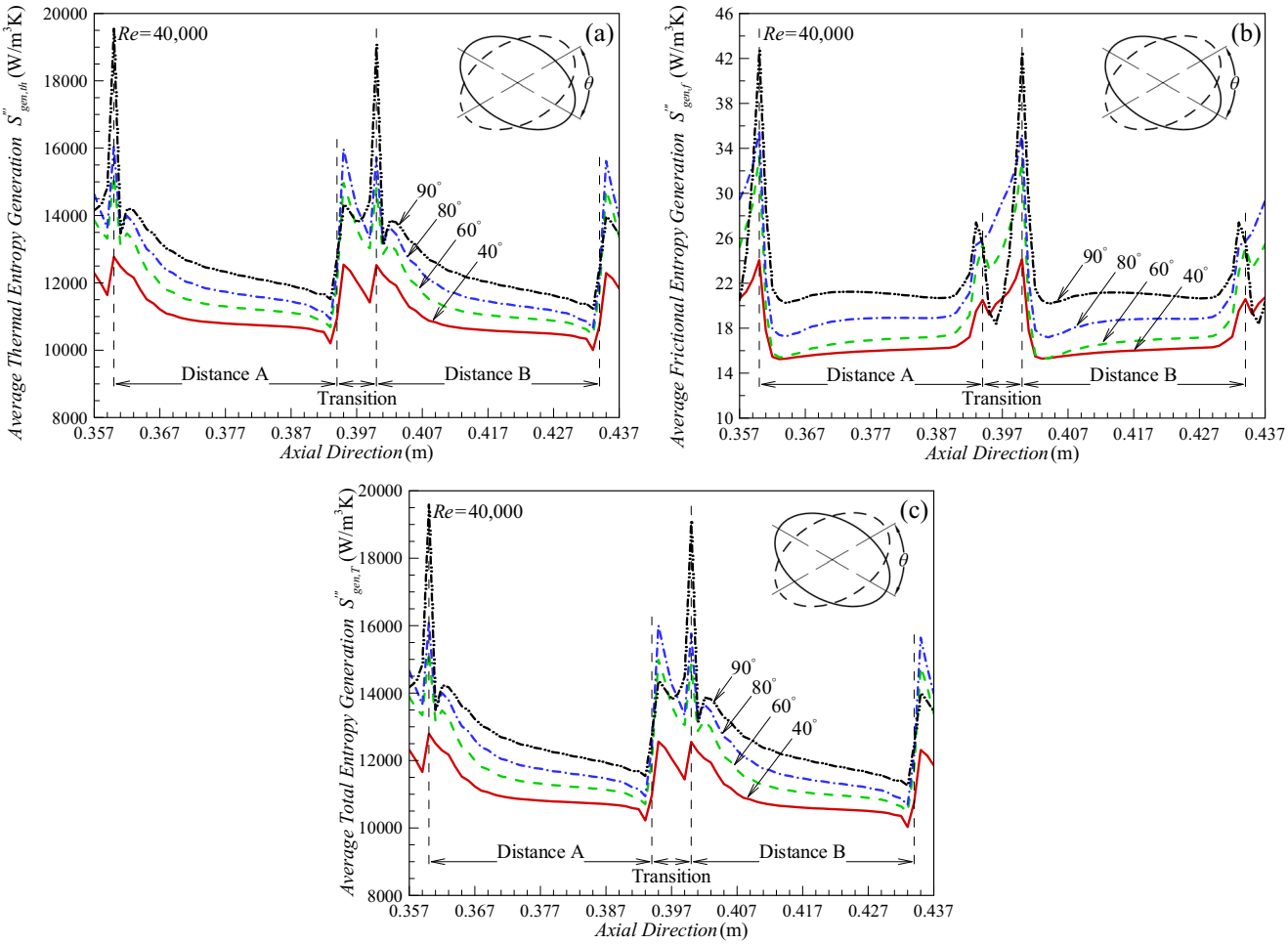

Fig. 15 Effect of different angles of θ on the average **a** thermal, **b** frictional and **c** total entropy generation along the axial direction of the AEA tubes

tubes. It is clear that the irreversibility is dominated by heat transfer. Furthermore, for all tubes, an increase in the Reynolds number resulted in a significant decrease in the Bejan number. Also, the Bejan number of AEA tube 40° is less than that of a circular tube and by increasing the angle of θ, the Bejan number decreased. It implies that frictional irreversibility is augmented by increasing the angle of θ compared to its smaller angles.

Figure 17 shows the ratio of total entropy generation of AEA tubes to that of circular tube ($S_{gen,T,AEAT}/S_{gen,T,CT}$) as a function of Reynolds number with different angles of θ. From Fig. 17, it can be seen that AEA tubes have higher total entropy generation than the circular tube at any Reynolds number. Besides, with the increase in Reynolds number after $Re = 20{,}000$, the total entropy generation percentages of AEA tube over the circular tube increases for all angles of θ. On the other hand, with the increase in Reynolds number from 10,000 to 20,000, ratio of $S_{gen,T,AEAT}/S_{gen,T,CT}$ decrease for all angles of θ. Therefore, according to this, the ratio of $S_{gen,T,AEAT}/S_{gen,T,CT}$ is minimum at around $Re = 20{,}000$. In the present study, at a Reynolds number of 20,000, $S_{gen,T,AEAT}/S_{gen,T,CT}$ were about 1.1086, 1.1484, 1.1765 and 1.2348 for angles of 40°, 60°, 80° and 90°. However, when the Reynolds number increases to 60,000, $S_{gen,T,AEAT}/S_{gen,T,CT}$ were only 1.1409, 1.1989, 1.2353 and 1.2762, respectively.

6 Conclusions

In this paper, a numerical study is performed to analyze the entropy generation and heat transfer enhancement of the AEA tubes in turbulent flow. The standard k-ε turbulence model is used, based on validation of the numerical results of different turbulence models with experimental results. The effect of different angles between pitches (θ) on the entropy generation of the AEA tubes have been investigated numerically.

Investigation of the streamlines indicated that the difference in angle of θ causes the change in number of multi-longitudinal vortices within the turbulent flow. The number of multi-longitudinal vortices are increased from four to eight with increasing the angle of θ from 60° to 80° at some part of constant cross-section of the AEA tube. Also, the multi-longitudinal vortices have a significant effect on heat transfer, pressure drop and entropy generation. For instance, on the

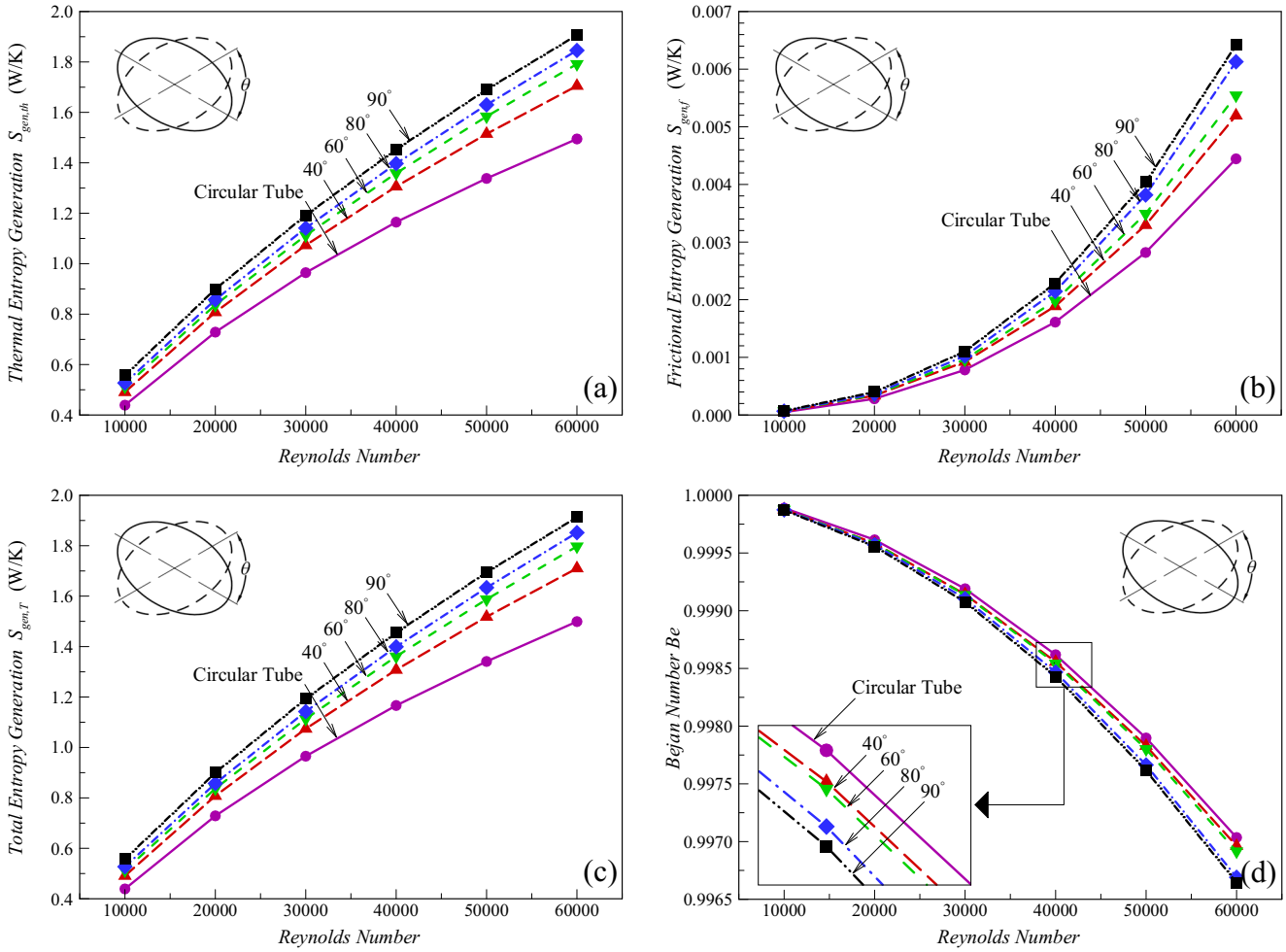

Fig. 16 Effect of increasing Reynolds number on the **a** thermal, **b** frictional, **c** total entropy generation and **d** Bejan number in AEA tubes and circular tube

positions of the tube wall that are close to the two symmetrical vortices with the same direction of rotation, the local wall shear stress and local total entropy generation are reduced.

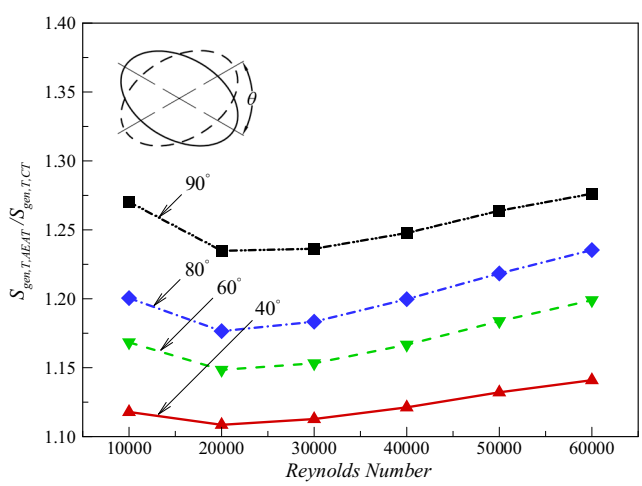

Fig. 17 Variations of $S_{gen,T,AEAT}/S_{gen,T,CT}$ with Reynolds number for AEA tubes with different angles of θ

But, the reduction of these parameters is not seen in many parts of the domain of the AEA tubes, due to the fact that such symmetrical vortices do not exist in some areas of the domains.

In addition, it has been observed that the average Nusselt number and friction factor of AEA tubes increases with an increment in Reynolds number and angle of θ. Also, the maximum amount of the *PEC* has been obtained at the lowest Reynolds number which its value is equal to 1.09 for the AEA tube 90°. The entropy generation analysis showed that the main source of irreversibility is thermal entropy generation. The increase of Reynolds number and angle of θ can increase the total entropy generation in AEA tubes as well as circular tubes. Moreover, the ratio of $S_{gen,T,AEAT}/S_{gen,T,CT}$ has been minimum at around the Reynolds number of 20,000. The entropy generation, which is caused by heat exchange and fluid friction losses, are changed with changing the angle of θ. A part of the novelty of this research is to study on the dissipated useful energy, and determining the losses of both terms (thermal and frictional) of the entropy. In a way that the

mechanical energy which comes from increasing the pressure drop is not wasted. This means that by alternating the cross-section of the elliptical tubes, how much is added to the irreversibility of the circular tube by increasing the pressure drop.

Compliance with ethical standards

Conflict of interest On behalf of all authors, the corresponding author states that there is no conflict of interest.

References

1. Javadpour A, Najafi M, Javaherdeh K (2018) Effect of magnetic field on forced convection heat transfer of a non-Newtonian nanofluid through an annulus: an experimental study. Heat Mass Transf 54(11):3307–3316. https://doi.org/10.1007/s00231-018-2361-z
2. Armaghani T, Esmaeili H, Mohammadpoor YA, Pop I (2018) MHD mixed convection flow and heat transfer in an open C-shaped enclosure using water-copper oxide nanofluid. Heat Mass Transf 54(6):1791–1801. https://doi.org/10.1007/s00231-017-2265-3
3. Abbaszadeh M, Ababaei A, Abbasian Arani AA, Abbasi Sharifabadi A (2017) MHD forced convection and entropy generation of CuO-water nanofluid in a microchannel considering slip velocity and temperature jump. J Braz Soc Mech Sci Eng 39(3): 775–790. https://doi.org/10.1007/s40430-016-0578-7
4. Hekmatipour F, Jalali M, Hekmatipour F, Akhavan-Behabadi MA, Sajadi B (2019) On the convection heat transfer and pressure drop of copper oxide-heat transfer oil Nanofluid in inclined microfin pipe. Heat Mass Transf 55(2):433–444. https://doi.org/10.1007/s00231-018-2417-0
5. Subhedar DG, Ramani BM, Gupta A (2018) Experimental investigation of heat transfer potential of Al_2O_3/Water-Mono Ethylene Glycol nanofluids as a car radiator coolant. Case Studies in Thermal Engineering 11:26–34. https://doi.org/10.1016/j.csite.2017.11.009
6. Moreira TA, Moreira DC, Ribatski G (2018) Nanofluids for heat transfer applications: a review. J Braz Soc Mech Sci Eng 40(6):303. https://doi.org/10.1007/s40430-018-1225-2
7. Liu S, Jin H, Song K, Wang L, Wu X, Wang L (2017) Heat transfer and pressure drop characteristics of the tube bank fin heat exchanger with fin punched with flow redistributors and curved triangular vortex generators. Heat Mass Transf 53(10):3013–3026. https://doi.org/10.1007/s00231-017-2044-1
8. Sinha A, Chattopadhyay H, Iyengar AK, Biswas G (2016) Enhancement of heat transfer in a fin-tube heat exchanger using rectangular winglet type vortex generators. Int J Heat Mass Transf 101: 667–681. https://doi.org/10.1016/j.ijheatmasstransfer.2016.05.032
9. Du B-C, He Y-L, Wang K, Zhu H-H (2017) Convective heat transfer of molten salt in the shell-and-tube heat exchanger with segmental baffles. Int J Heat Mass Transf 113:456–465. https://doi.org/10.1016/j.ijheatmasstransfer.2017.05.075
10. Kumar R, Kumar A, Sharma A, Chauhan R, Sethi M (2017) Experimental study of heat transfer enhancement in a rectangular duct distributed by multi V-perforated baffle of different relative baffle width. Heat Mass Transf 53(4):1289–1304. https://doi.org/10.1007/s00231-016-1901-7
11. Mashoofi N, Pourahmad S, Pesteei SM (2017) Study the effect of axially perforated twisted tapes on the thermal performance enhancement factor of a double tube heat exchanger. Case Studies in Thermal Engineering 10:161–168. https://doi.org/10.1016/j.csite.2017.06.001
12. Abdelatief MA, Sayed Ahmed SAE, Mesalhy OM (2018) Experimental and numerical study on thermal-hydraulic performance of wing-shaped-tubes-bundle equipped with winglet vortex generators. Heat Mass Transf 54(3):727–744. https://doi.org/10.1007/s00231-017-2164-7
13. Li B, Feng B, He Y-L, Tao W-Q (2006) Experimental study on friction factor and numerical simulation on flow and heat transfer in an alternating elliptical axis tube. Appl Therm Eng 26(17):2336–2344. https://doi.org/10.1016/j.applthermaleng.2006.03.001
14. Sajadi AR, Yamani Douzi Sorkhabi S, Ashtiani D, Kowsari F (2014) Experimental and numerical study on heat transfer and flow resistance of oil flow in alternating elliptical axis tubes. Int J Heat Mass Transf 77:124–130. https://doi.org/10.1016/j.ijheatmasstransfer.2014.05.014
15. Najafi Khaboshan H, Nazif HR (2018) Heat transfer enhancement and entropy generation analysis of Al_2O_3-water nanofluid in an alternating oval cross-section tube using two-phase mixture model under turbulent flow. Heat Mass Transf 54(10):3171–3183. https://doi.org/10.1007/s00231-018-2345-z
16. Siavashi M, Jamali M (2016) Heat transfer and entropy generation analysis of turbulent flow of TiO_2-water nanofluid inside annuli with different radius ratios using two-phase mixture model. Appl Therm Eng 100:1149–1160. https://doi.org/10.1016/j.applthermaleng.2016.02.093
17. Oztop HF, Al-Salem K (2012) A review on entropy generation in natural and mixed convection heat transfer for energy systems. Renew Sust Energ Rev 16(1):911–920. https://doi.org/10.1016/j.rser.2011.09.012
18. Al-Zamily AMJ (2017) Analysis of natural convection and entropy generation in a cavity filled with multi-layers of porous medium and nanofluid with a heat generation. Int J Heat Mass Transf 106:1218–1231. https://doi.org/10.1016/j.ijheatmasstransfer.2016.10.102
19. Hussain S, Mehmood K, Sagheer M (2016) MHD mixed convection and entropy generation of water–alumina nanofluid flow in a double lid driven cavity with discrete heating. J Magn Magn Mater 419:140–155. https://doi.org/10.1016/j.jmmm.2016.06.006
20. Zhao L, Liu LH (2010) Entropy generation analysis of electro-osmotic flow in open-end and closed-end micro-channels. Int J Therm Sci 49(2):418–427. https://doi.org/10.1016/j.ijthermalsci.2009.07.009
21. Jafarmadar S, Azizinia N, Razmara N, Mobadersani F (2016) Thermal analysis and entropy generation of pulsating heat pipes using nanofluids. Appl Therm Eng 103:356–364. https://doi.org/10.1016/j.applthermaleng.2016.03.032
22. Chahartaghi M, Eslami P, Naminezhad A (2018) Effectiveness improvement and optimization of shell-and-tube heat exchanger with entransy method. Heat Mass Transf 54(12):3771–3784. https://doi.org/10.1007/s00231-018-2401-8
23. Elsayed ML, Mesalhy O (2015) Studying the performance of solid/perforated pin-fin heat sinks using entropy generation minimization. Heat Mass Transf 51(5):691–702. https://doi.org/10.1007/s00231-014-1451-9
24. Bouras F, Khaldi F (2016) Computational modeling of thermodynamic irreversibilities in turbulent non-premixed combustion. Heat Mass Transf 52(4):671–681. https://doi.org/10.1007/s00231-015-1587-2
25. You Y, Fan A, Liang Y, Jin S, Liu W, Dai F (2015) Entropy generation analysis for laminar thermal augmentation with conical strip inserts in horizontal circular tubes. Int J Therm Sci 88:201–214. https://doi.org/10.1016/j.ijthermalsci.2014.10.003
26. Ko T, Wu C (2009) A numerical study on entropy generation induced by turbulent forced convection in curved rectangular ducts with various aspect ratios. International Communications in Heat

and Mass Transfer 36(1):25–31. https://doi.org/10.1016/j.icheatmasstransfer.2008.08.016
27. Siadaty M, Kazazi M (2018) Study of water based nanofluid flows in annular tubes using numerical simulation and sensitivity analysis. Heat Mass Transf 54(10):2995–3014. https://doi.org/10.1007/s00231-018-2339-x
28. Ebrahimi A, Rikhtegar F, Sabaghan A, Roohi E (2016) Heat transfer and entropy generation in a microchannel with longitudinal vortex generators using nanofluids. Energy 101:190–201. https://doi.org/10.1016/j.energy.2016.01.102
29. Zheng N, Liu P, Shan F, Liu Z, Liu W (2016) Numerical investigations of the thermal-hydraulic performance in a rib-grooved heat exchanger tube based on entropy generation analysis. Appl Therm Eng 99:1071–1085. https://doi.org/10.1016/j.applthermaleng.2016.02.008
30. White FM (1991) Viscous fluid flow, 2nd edn. McGraw-Hill, New York
31. Guo ZY (2003) A brief introduction to a novel heat-transfer enhancement heat exchanger. Department of EMEMKLEHTEC, Tsinghua University, Beijing
32. Najafi Khaboshan H, Nazif HR (2018) The effect of multi-longitudinal vortex generation on turbulent convective heat transfer within alternating elliptical axis tubes with various alternative angles. Case Studies in Thermal Engineering 12:237–247. https://doi.org/10.1016/j.csite.2018.04.013
33. Najafi Khaboshan H, Nazif HR (2018) Investigation of heat transfer and pressure drop of turbulent flow in tubes with successive alternating wall deformation under constant wall temperature boundary conditions. J Braz Soc Mech Sci Eng 40(2):42. https://doi.org/10.1007/s40430-017-0935-1
34. Sajadi AR, Kowsary F, Bijarchi MA, Sorkhabi SYD (2016) Experimental and numerical study on heat transfer, flow resistance, and compactness of alternating flattened tubes. Appl Therm Eng 108:740–750. https://doi.org/10.1016/j.applthermaleng.2016.07.033
35. Meng J-A, Liang X-G, Chen Z-J, Li Z-X (2005) Experimental study on convective heat transfer in alternating elliptical axis tubes. Exp Thermal Fluid Sci 29(4):457–465. https://doi.org/10.1016/j.expthermflusci.2004.04.006
36. Chen W-L, Guo Z, Chen C-K (2004) A numerical study on the flow over a novel tube for heat-transfer enhancement with a linear Eddy-viscosity model. Int J Heat Mass Transf 47(14):3431–3439. https://doi.org/10.1016/j.ijheatmasstransfer.2004.01.014
37. Shah RK, London AL (1978) Laminar Flow Forced Convection in Ducts. Academic Press, London
38. Launder BE, Spalding DB (1972) Lectures in Mathematical Models of Turbulence. Academic Press, London
39. Bejan A (2013) Convection heat transfer, 4th edn. John Wiley & Sons, Hoboken
40. Bejan A (1982) Entropy generation through heat and fluid flow. Wiley, New York
41. Holmes DG, Connell SD (1989) Solution of the 2D Navier-Stokes equations on unstructured adaptive grids. In: 9th Computational Fluid Dynamics Conference, AIAA p1932
42. Rausch RD, Batina JT, Yang HTY (1991) Spatial adaption procedures on unstructured meshes for accurate unsteady aerodynamic flow computation. In: 32nd Structures, Structural Dynamics, and Materials Conference. AIAA, p 1106
43. Van Doormaal JP, Raithby GD (1984) Enhancements of the SIMPLE method for predicting incompressible fluid flows. Numerical Heat Transfer 7(2):147–163. https://doi.org/10.1080/01495728408961817
44. Chorin AJ (1968) Numerical solution of the Navier-Stokes equations. Math Comput 22(104):745–762. https://doi.org/10.1090/S0025-5718-1968-0242392-2
45. Versteeg HK, Malalasekera W (2007) An introduction to computational fluid dynamics: the finite volume method, 2nd edn. Pearson Education, London
46. Warming RF, Beam RM (1976) Upwind second-order difference schemes and applications in aerodynamic flows. AIAA J 14(9):1241–1249. https://doi.org/10.2514/3.61457
47. Launder BE, Spalding DB (1974) The numerical computation of turbulent flows. Comput Methods Appl Mech Eng 3(2):269–289. https://doi.org/10.1016/0045-7825(74)90029-2
48. Gnielinski V (1976) New equations for heat and mass transfer in turbulent pipe and channel flow. Int Chem Eng 16(2):359–368
49. Bergman TL, Lavine AS, Incropera FP, Dewitt DP (2011) Fundamentals of heat and mass transfer, 7th edn. John Wiley & Sons, Hoboken
50. Petukhov BS, Irvine TF, Hartnett JP (1970) Advances in Heat Transfer. Academic Press, New York
51. Webb RL, Kim N-H (1994) Principles of enhanced heat transfer. Taylor Francis, New York

Publisher's note Springer Nature remains neutral with regard to jurisdictional claims in published maps and institutional affiliations.